ORNL/TM--9175

DE84 014415

Fusion Energy Division

THE EBT-S 28-GHz, 200-kW, CW, MIXED-MODE, QUASI-OPTICAL PLASMA HEATING SYSTEM

T. L. White
H. D. Kimrey
T. S. Bigelow
D. D. Bates
H. O. Eason*

Date Published - July 1984

*Deceased.

NOTICE This document contains information of a preliminary nature. It is subject to revision or correction and therefore does not represent a final report.

Prepared by the
OAK RIDGE NATIONAL LABORATORY
Oak Ridge, Tennessee 37831
operated by
MARTIN MARIETTA ENERGY SYSTEMS, INC.
for the
U. S. DEPARTMENT OF ENERGY
under Contract No. DE-AC05-840R21400

EB

CONTENTS

Abstract

The ELMO Bumpy Torus-Scale (EBT-S) 28-GHz, 200-kW, cw, plasma heating system consists of a gyrotron oscillator, an oversized waveguide two-bend transmission system, and a quasi-optical mixed-mode microwave distribution manifold that feeds microwave power to the 24 plasma loads of the EBT-S fusion experiment. Balancing power to the 24 loads was achieved by adjusting the areas at 24 coupling irises. System performance is easily measured using system calorimetry. The distribution manifold mixed-mode power transmission, reflection, and loss coefficients are 89%, 6%, and 5%, respectively. The overall system efficiency (plasma power/gyrotron power) is 80%, but with some modifications to the distribution manifold we believe the ultimate efficiency can approach 90%. The system reliability is outstanding with a world's record 1×10^5 kW·h of 28-GHz energy delivered to the EBT-S device with well over 1×10^3 operating hours.

I. Introduction

The ELMO Bumpy Torus-Scale (EBT-S) fusion experiment[1] consists of 24 simple magnetic mirrors joined end-to-end to form a torus of closed magnetic field lines. A plasma is created, stabilized, and heated by the application of 28-GHz, 200-kW, cw electron cyclotron heating (ECH) power from commercially available gyrotron oscillators.[2] The availability of these tubes was the direct result of an intensive gyrotron development program in private industry[3] initiated by the EBT program to address the need for higher-frequency, high-power sources essential to demonstrate scaling of the fusion-relevant toroidal plasma in EBT-I.[4] The end result of this development effort was the delivery of reliable 200-kW, cw axisymmetric gyrotron oscillators with good efficiency (≤50%) and with somewhat relaxed constraints on mode purity (primarily TE^{o}_{02} with some TE^{o}_{01} and TE^{o}_{03} modes). In parallel with the 28-GHz gyrotron development program, a component development effort was undertaken at Oak Ridge National Laboratory (ORNL) in the EBT group to provide the necessary high-power oversized waveguide components to transmit and distribute the ECH power to the 24 plasma cavities of the EBT-S device. Much of the high-power experience gained in earlier development efforts[5] on the ELMO device[6] with 5 kW of cw ECH power at 35 and 55 GHz was used in the development of the EBT-S ECH system. Although there is a large volume of literature available on work done by Bell Laboratories on oversized waveguide systems[7] communication systems[8] and by others on high-power radar, these applications requirements are different from the EBT-S requirements of very good reliability at high average power, 24-way power division, and relaxed mode control. These differences necessitated a unique design approach for the EBT-S ECH system.

II. Design Criteria

Because ECH is the primary heating scheme on EBT-S, great emphasis is given to good reliability for the ECH system. Ease of fabrication, maintenance, and operation are also desirable characteristics for the system. Every component must have high average power handling capability, which requires precision waveguide tolerances at flange joints to ensure metal-to-metal contact, polished low-loss internal metallic surfaces, and adequate cooling. The microwave system as a whole must produce low reflected power in any mode at the gyrotron, especially in circular electric modes, which can interact strongly with the gyrotron cavity mode. Low reflections result in smooth operation at the gyrotron oscillator without frequency jumping and low dissipation in the gyrotron body, collector seal, and window cooling circuits.

Reflections should also be kept to a minimum to reduce the effect of trapped (spurious) mode resonances. These resonances are caused by irregularities such as bends and flange offsets separated by an integer number of half-guide wavelengths for a particular trapped mode. A cavity is thus formed that can transfer energy from the main mode to the trapped mode if the phases of the two modes are properly adjusted.[9] This will cause local heating in the trapped region and even arcing, as well as a frequency sensitive reduction in transmission efficiency. This situation can be prevented by applying two techniques. First, exciting the spurious modes must be avoided by carefully controlling the waveguide shape. Second, if spurious mode excitation cannot be avoided, as in the case of a bend, then any spurious mode that is excited must be allowed to propagate freely without reflection toward the plasma, where it can be absorbed. This is feasible since higher-order mode power is useful for plasma heating in EBT-S.[10] Elements of both techniques are used in the EBT-S ECH system. In addition, all forward mode converted power must be allowed to propagate to each of the 24 ECH loads in a balanced manner.

III. System Description

The ECH system can be broken into transmission and distribution subsystems as shown in Fig. 1. The transmission system consists of a VGA-8000 axisymmetric gyrotron oscillator,[11] arc detectors, spurious mode absorbers, two 90° curved bends, a waveguide run to a vacuum window, and a waveguide run through a bellows feeding a power splitter into the distribution system. The gyrotron output waveguide is 6.35 ± 0.005-cm-I.D. high conductivity copper, and this diameter is maintained throughout the transmission system to preclude any reflections. The wall thickness is 4.76 mm and is determined by the waveguide flange design, to be described later, as well as mechanical strength and cooling considerations. The waveguide is pressurized at 1 psig of dry nitrogen to prevent the entry of foreign matter and moisture into the system. The nitrogen atmosphere is fed into the system from the lowest points and removed with a pressure relief valve at the highest point. This allows the waveguide atmosphere to be replenished every few hours. The pressure is also interlocked as a safety measure to inhibit operation if a gross nitrogen leak is present, which indicates waveguide joint misalignment and therefore microwave leakage. Flange joints are surveyed periodically with a hand-held isotropic radiation monitor as an additional safety precaution. The entire system is water cooled to protect components from excessive temperature increases characteristic of high average power operation, and for personnel safety considerations. Water cooling is also required for system calorimetry[12] to measure gyrotron output power as well as transmission losses.

The arc detector waveguide section located above the gyrotron window (shown in Fig. 2) has a number of functions. Photoelectric and acoustic arc detectors (as well as a gas feed and a frequency sampler) are coupled to the oversized waveguide via cutoff holes. The main protection for the gyrotron window is a fast, 5-μs, commercially available photoelectric arc detector, which senses light produced by a waveguide arc in the system through a fiber optic light pipe inserted at an angle to the waveguide axis looking at the gyrotron output window. A test light signal is also injected at the mounting block to verify proper operation of the entire arc detector system. In normal operation, waveguide arcs are very infrequent (usually only a few per year) and are nearly always caused by foreign matter falling on the outer ceramic disk of the windows. These particles are usually microscopic metal slivers caused by the assembly of the metal-to-metal waveguide joints during system maintenance. To minimize these slivers, the arc detector section is always the last section to be replaced to facilitate window cleaning with a small vacuum hose.

The acoustic arc detector is used primarily for arc location[13] in conjunction with an identical detector located at the other end of the pressurized waveguide system near the barrier window. The acoustical pickup is a standard audio microphone chosen for its high-frequency response and low output impedance. The difference in the time of arrival of the acoustical signal between the two detectors is a direct measure of the position of the arc. This arc detector is very useful for locating problem areas in new components that are occasionally tested in our system.

The frequency sampler is a dominant mode WR-28 waveguide tangent to the circular waveguide with coupling achieved by a hole in cutoff at the

tangent point. This configuration is best for sampling both TE and TM modes through the Er, Hϕ, and Hz wall components in the circular guide which couple to the Ey, Hz, and Hx components, respectively, in the dominant mode waveguide. One end of the WR-28 waveguide is matched while the other end feeds a 50-ft run of waveguide to the control room, where a microwave counter, spectrum analyzer, wavemeter and broadband detector serve to measure the gyrotron frequency in the 26.5- to 40-GHz range. The wide bandwith is necessary to detect spurious frequencies occasionally generated by the gyrotron during startup or high-power operation.

The arc detector waveguide section also serves as an adaptor section between the gyrotron flange and the ORNL waveguide flange design. The ORNL flange is shown in Fig. 3 and is designed to be a sexless metal-to-metal waveguide joint for flexibility and reliability. The clamping rings are held to the waveguide by a stainless steel snap ring, and transverse alignment of the waveguide joint is accomplished by a split alignment ring. The alignment ring is split for transverse insertion of the last waveguide section between fixed ends and to verify proper alignment of the last waveguide flange joint in the system before joint assembly. The metal-to-metal contact at the inside diameter is ensured by relieving the face of the mating surface. The clamping rings are completely rotatable and play no role in precise transverse alignment. The design is easy to fabricate, reliable, rugged, and very easy to install.

Two kinds of mode absorbers are used to protect the gyrotron from excessive reflections. Commercially available high average power mode absorbers[14] consist of equally spaced circular copper rings. The gap between the rings is equal to a ring thickness. The rings are surrounded by an alumina tube backed with water to absorb the noncircular electric mode power that propagates radially outward between adjacent rings. Circular electric modes have very low insertion losses in this absorber because of their wall currents, which follow the rings circumferentially. The disadvantage of the spaced ring configuration is that, to couple out appreciable power in spurious modes, the gaps have to be on the order of a quarter-guide wavelength, and resonant reflections can be a problem if the ring period is equal to a half-guide wavelength.[15] In addition, large gaps tend to preferentially excite higher-order circular electric modes if a lower-order circular electric mode illuminates the gaps.[16] For these reasons, we have added a length of stainless steel waveguide between the gyrotron and the spaced ring mode absorber to damp potential reflections from the spaced ring absorbers. The stainless steel waveguide also has some mode filtering properties, since the circular electric modes have the smallest losses compared to most other modes or mode families.

Changes in the direction of the waveguide transmission system are accomplished by two identical 90° curved bends, one of which is shown in Fig. 4. The first bend directs the vertical gyrotron output horizontal while the second bend directs the power vertically downward to the distribution system. The bends have a 40.6-cm constant radius of curvature and were rolled from straight, annealed waveguide sections filled with a bismuth bending alloy for internal support. The ovality of the 6.35-cm waveguide was less than ±0.76 mm. These bends were chosen over earlier miter bends[17] because of very low reflections for large classes of waveguide modes. In cold test with a TE°_{01} mode incident on the bend, the multimode reflections from a single curved

bend are equivalent to a 0.4-mm flange offset in a 6.35-cm-I.D. waveguide joint. The cold test technique used and the data generated are presented in the appendix. Curved bends also tend to severely forward convert the incident circular electric modes into complex mixtures of TE^{o}_{on} and TM^{o}_{1n} degenerate mode pairs as well as nondegenerate (TE^{o}_{1n}, TE^{o}_{2n}, . .) spurious modes.[18] However, this was not deemed to be a problem since mode control is not a requirement for the EBT-S ECH system.

The complex mix of modes produced by the curved bends is fed through a vacuum window (similar to the gyrotron output window[19]) that isolates the pressurized waveguide transmission system from the EBT-S vacuum. The window consists of two BeO (or Al_2O_3) ceramic disks separated by a gap with FC-75 dielectric fluid circulated in the gap for face cooling the ceramic disks. Several turns of polyethelyene tubing filled with circulating water are wrapped outside of the ceramic disks to load noncircular electric mode microwave power, which tends to radiate out in the gap between the ceramic disks. After the window, the 6.35-cm-I.D. waveguide passes through a bellows so that the first-pass microwave power does not reflect off the bellows corrugations. The dimensions of the bellows are 9.53-cm length, 13.2-cm I.D. with a 19.1-mm period, and a 8.3-mm corrugation depth. Tne bellows was designed to preclude arcing in a mixed-mode microwave environment. This results in a rather stiff bellows with shallow and widely spaced corrugation, compared to a wavelength. This bellows allows flexibility for mechanical adjustments during assembly of the vertical input waveguide to the microwave distribution system.

The microwave distribution system shown in Fig. 5 is a modified version of the original stainless steel, toroidal vacuum pumping manifold (R = 1.02 m, r = 10.2 cm) used on the earlier EBT-I device. That manifold was coupled to the 24 plasma cavities of the device through twenty-four 15.3-cm-I.D. feeds, and four large vacuum pumps equally spaced around the manifold served to evacuate the device. The pumps were isolated from the 10.6- and 18-GHz power used in EBT-I by having a 15.3-cm-diam metal plate perforated with a very large number of circular holes in cutoff located at each of the 24 cavity feeds.

Several modifications allowed this vacuum manifold to also serve as the 28-GHz microwave distribution system. Internal sharp corners and points that might tend to arc in the presence of high power microwaves were removed or radiused where appropriate. Also, internal stainless steel surfaces were plated with copper to reduce the microwave losses. Each of the 24 cavity cutoff screens had a circular hole or iris (of varying diameters) bored through it to balance the distribution of microwave power to each of the 24 plasma cavities, and a large cutoff screen was placed over each vacuum pump to maintain microwave isolation. Finally, all standard O-ring grooves on the vacuum manifold were protected from direct microwave heating by providing a metal-to-metal interference fit[20] between the microwave power and the O-ring groove.

The input power to the manifold is split and scattered toroidally in opposite directions by a "Y-splitter," shown in Fig. 5. The Y-splitter is a three-port, mixed-mode junction formed by joining two identical curved bends with one end of each bend facing in opposite directions and the other two ends joined together to form a common input. The Y-splitter splits the manifold

input power into two roughly equal parts for scattering in toroidally opposite directions in the manifold. The dimensions of the manifold are much much greater than a wavelength and can therefore contain a very large number of possible modes, which are excited by irregular shapes in the manifold such as cavity and vacuum pump feeds.

At each iris an amount of power roughly equal to 1/24th of the power delivered to the entire device is coupled out. This is accomplished by tapering up the iris areas going away from the manifold input in a symmetrical fashion. Using a Monte Carlo ray tracing code[21] to simulate microwave transport in oversized, quasi-optical geometries, an optimum coupling distribution was computed that gave a maximum total coupling area with a balanced distribution of power, and reduced the manifold losses from 10% to 5%. Table I lists the iris diameters for all 24 cavities.

The vacuum manifold approach to mixed-mode microwave power distribution was employed because (1) mode control is not an EBT-S ECH system requirement; (2) the first cw, 28-GHz gyrotrons that became available were of the triple miter variety that produce a wide variety of modes which would not be compatible with a mode controlled system; (3) power division in a mixed-mode system is relatively easy compared to a mode controlled approach, given that the ray tracing codes necessary to optimize the irises are developed; (4) combining the vacuum and microwave distribution into a single manifold maximizes the cost-effective use of an existing structure where available space is scarce; and (5) a single barrier window on the manifold input is cheaper, more quickly implemented, and much more reliable than having a pressurized microwave manifold with 24 specialized high-power windows. The disadvantage of this approach is that changes in the 24 iris sizes require a vacuum opening and several days to implement.

TABLE I. Iris diameters for all 24 cavities.

Cavity No.	Area (cm^2)	Remarks
W1	31.2	
W2	34.0	
W3	38.5	
W4	44.9	
W5	53.6	
W6	65.3	
N1	79.4	
N2	97.1	
N3	63.9	Area limited by diagnostic interference
N4	122.7	
N5	125.0	
N6	126.6	
E1	119.2	
E2	0	Intentionally unfed for diagnostic requirements
E3	114.3	
E4	108.1	
E5	98.9	
E6	88.5	
S1	78.2	
S2	67.6	
S3	57.9	
S4	48.7	
S5	38.8	
S6	30.9	

IV. System Performance

The gyrotron output power is measured calorimetrically by obtaining a flow and a temperature rise between the supply and return on all gyrotron cooling circuits, which directly yields the power dissipated in the gyrotron. These heat losses are subtracted from the total electrical input power of the gyrotron electron beam (heater and modulating anode power are negligible by comparison) to yield the microwave power propagating out of the gyrotron given by

$$P_g = V_B I_B - c(F_c \Delta T_c + F_b \Delta T_b + F_{cs} \Delta T_{cs}) - c' F_w \Delta T_w, \quad (1)$$

where

P_g = gyrotron output power in kW,

V_B = beam voltage in kV,

I_B = beam current in A,

c = 0.0696 kW/L/m – °C for H_2O,

c' = 0.0307 kW/L/m – °C for FC-75,

F = coolant flow in L/m,

ΔT = temperature difference beween inlet and outlet coolant in °C,

and the subscripts c, b, cs, and w refer to the gyrotron collector, body, collector seal, and window cooling circuits, respectively. The gyrotron output power calculated in this way is sensitive to systematic measurement errors, and great care must be taken to ensure that these errors are minimized by the use of precision voltage dividers and current shunts and by exercising good calorimetric practice in monitoring the various heat loads in the gyrotron.

The self-consistency of Eq. (1) can be verified by producing an electron beam at sufficiently low transverse energy to preclude microwave power generation. Then, the beam input power should equal the heat losses. As the transverse energy is raised, the oscillation threshold of the TE^o_{02} mode is reached and the collector power starts to drop, since transverse beam energy is converted to microwaves. A matched water load[22] placed at the end of the transmission system serves to absorb all gyrotron output power, and the agreement between the gyrotron output power given by Eq. (1) and the power delivered to a dummy load plus transmission system losses is within ±2 kW, as shown in Fig. 6. The power to the EBT-S plasma is inferred by monitoring calorimetrically each transmission and distribution component and subtracting the sum from the gyrotron power, given by

$$P_p = P_g - \Sigma_i P_{L_i} , \quad (2)$$

where

P_p = EBT-S plasma power in kW,

P_{L_i} = i^{th} waveguide component loss in kW .

This calorimetric power measurement technique is not dependent on mode content as long as all internal waveguide surfaces are properly cooled and

instrumented. Reflections from the plasma are also accounted for by system calorimetry, so that Eq. (2) represents the net power delivered to the plasma. Recently, a computer code has been implemented that monitors each of the parameters in Eqs. (1) and (2). Component losses in the gyrotron and the transmission and distribution system are displayed every 2 s, along with the gyrotron power, microwave power conversion efficiency, gyrotron frequency, and plasma power. Losses are also displayed as a percentage of gyrotron power.

The bar graph in Fig. 7 compares the power absorbed in each component relative to gyrotron output power comparing plasma operation with operation into a matched load. The spaced ring mode absorber and stainless steel mode absorber are abbreviated as VMA and SSMA, respectively. The numbers are an average of data points taken over a wide range of gyrotron operating conditions. The system efficiency, as measured by power delivered to the plasma divided by gyrotron power, is ~80%. This compares with ~95% efficiency for disconnecting the barrier window and manifold and connecting a matched water load. The increased power absorbed in the waveguide and in the mode absorbers during plasma operation is due to reflections and losses from the barrier window and manifold. Note here that the losses in the mode absorbers and waveguide increase in the presence of the reflection whereas the gyrotron losses remain relatively unchanged. This shows that the mode absorbers adequately absorb the reflected power in a single pass, allowing the gyrotron to operate relatively isolated from the mismatch of the window/manifold combination.

In order to determine the reflection coefficient of the barrier window and manifold, a simple model based on first-pass incident power and single-pass reflected power will be developed. The model neglects trapped resonances due to small misalignments in waveguide joints and will assume that the radiused bends have a negligible reflection coefficient compared to the window or the manifold. Three cases of hot test data must be run:

Case A: running the gyrotron into the transmission system terminated by a matched load.

Case B: Case A with the barrier window inserted just before the matched load.

Case C: EBT-S plasma operation.

Hot test data collected for each of the three runs are plotted in Figs. 8 and 9 for mode absorber plus copper waveguide losses and window losses, respectively. In the following analysis, we assume that

$$P_{in} = P_{in}(R + L + T) \quad , \tag{3}$$

where P_{in} is the incident power for the component in question and R, L, and T are the mixed-mode power reflection, loss, and transmission coefficients, respectively. The losses in various components are a linear function of gyrotron power, indicating that no mode-sensitive effects exist as has been noted in the past when operating with miter bends.

For Case A, assuming that the matched load produces negligible reflections,

$$P_g = P^A_L + P^A_{Load} \quad , \tag{4}$$

where P^A_L is the combined losses of the mode absorbers and copper waveguide and P^A_{Load} is the power absorbed in the matched load for Case A.

In Case B,

$$P_g = P^B_L + P^B_W + P^B_{Load} \quad , \tag{5}$$

where P^B_W is the combined loss of the barrier window FC-75 and H_2O cooling circuits. Assuming that the increase in transmission system losses is due to a single-pass reflection from the barrier window, then

$$P^B_L = P^A_L + (P_g - P^A_L)R_W \quad . \tag{6}$$

The second term in Eq. (6) is the power reflected by the window and R_W is the normalized window reflection coefficient. Rearranging Eq. (6) yields the window reflection coefficient:

$$R_W = (P^B_L - P^A_L)/(P_g - P^A_L) \quad . \tag{7}$$

In the same manner, analyzing Case C,

$$P_g = P^C_L + P^C_W + P^C_L \quad , \tag{8}$$

where P^C_L is now the inferred plasma power plus the manifold losses.

The increased transmission system losses are written

$$P^C_L = P^A_L + (P_g - P^A_L)R_W + (P_g - P^A_L - P^B_W)R_M - (P^C_W - P^B_W) \quad , \tag{9}$$

where the second term is the window reflection, the third term is manifold and plasma reflection, and the fourth term represents manifold reflection absorbed by the window. Rearranging Eq. (9) to solve for R_M, we have

$$R_M = (P^C_L - P^B_L + P^C_W - P^B_W)/(P_g - P^A_L - P^B_W) \quad . \tag{10}$$

Applying the data in Figs. 8 and 9 to Eqs. (7) and (10) yields $R_W \approx 1.7\%$ and $R_M \approx 6.0\%$.

Considering that the short radius bends generate a mix of noncircular electric modes, R_W is surprisingly small for a barrier window designed for the TE^o_{02} mode. The low reflections from the barrier window imply that most of the forward converted modes are at or near the TE^o_{02} mode propagation constant (for example TM^o_{12}, TE^o_{22}, etc.); otherwise their match to the window would be much worse than measurements indicate. The manifold reflections are probably due to backscattering off of vacuum pump cutoff screens and off cavity feeds that have iris diameters less than the full feed diameter. These reflections probably originate near the input where multiple-pass cavity coupling is not able to isolate reflections. These reflections can be minimized by placing the vacuum cutoff screens and coupling irises flush with the toroidal manifold inside dimensions. We estimate that the manifold reflections can be reduced to ~2% by this method.

V. Conclusions

We have developed accurate, mode-independent calorimetric techniques to measure cw gyrotron output power as well as system efficiency into a plasma load. The individual component losses are easily measured directly, and the system transmission efficiency is inferred by subtracting total losses from gyrotron output power to yield a respectable 80%. By measuring system losses for different matched and plasma load configurations, we can indirectly measure the mixed-mode reflection coefficients. The distribution manifold transmission, absorption, and reflection coefficients are found to be 89%, 5%, and 6%, respectively, using this technique. The ultimate efficiency of the ECH system could be 90% by removing the vacuum barrier window and redesigning the manifold. This would require a slight redesign of the waveguide flange to accommodate O-ring vacuum seals. Also, a pumping scheme for the waveguide transmission system would have to be devised. Finally, the system has demonstrated outstanding reliability for delivery of ECH power to the EBT-S plasma experiment. At this writing, there are over 1×10^5 kW·h of 28-GHz energy delivered to the EBT-S plasma with total operations exceeding 1×10^3 hours. This amount of energy delivered is a world record. In general, the ECH system reliability is limited by high-voltage power supply reliability and not by the gyrotron and waveguide component reliability.

APPENDIX – The Trapped Resonance Method for Qualitative Measurement of Reflections from Oversized Waveguide Components

The test set up used for measurement is shown in Fig. 10. A leveled backward wave oscillator sweeper feeds a Lanciani[23] $TE^{\square}_{10} \rightarrow TE^{o}_{01}$ mode transducer that produces a fairly pure output over a 10% bandwidth if a companion mode absorber is used to damp spurious modes excited by the transducer. A two-section linear taper designed after Solymar[24] was used to taper up the waveguide diameter to 6.35 cm. A TE mode coupler (shown in Fig. 11) consists of a dominant mode WR-28 waveguide oriented along a radius of the oversized waveguide. The broad wall of the rectangular waveguide is parallel to the axis of the oversized waveguide and a 6-dB coupling hole couples only the Hz fields in the oversized waveguide into Hx field in the dominant mode rectangular waveguide. All other E and H field components in the oversized waveguide either are zero at the wall (E_z, E_ϕ) or do not have corresponding fields in the rectangular guide (H_r, H_ϕ, E_r). A broadband isolator damps reflections between the 6-dB coupling hole and a broadband detector. The detector isolator combination serves to produce a fairly flat frequency response when the TE^{o}_{01} mode radiates into free space or a matched load. The first-pass free-space frequency response of the TE mode coupler is stored as a reference in the digital memory of a network analyzer. When a component is placed between the TE coupler and free space, the reference sweep begins to distort due to reflections from the component under test. These reflections are frequently in modes different than the forward going TE^{o}_{01} mode and are trapped in resonance between the taper and the component under test The TE mode coupler is rotated azimuthally about the 6.35-cm waveguide, and maximum coupling to the reflected modes occurs when the coupling hole is in the plane of the bends. This sweep is normalized to the reference for free space and the results are shown in Fig. 12 for a 90°, 6.35-cm-I.D. miter bend (solid curve) and a 90°, 45.7-cm radius of curvature bend in the 6.35-cm-I.D. waveguide (dashed curve).

The miter bend reflections are 10 to 16 dB higher than free-space response, and the radius bend produces only about ± 1 dB fluctuation about free space. To relate this to a familiar waveguide perturbation, we produced a small 0.4-mm flange offset in the same plane as the bends that achieved nearly the same fluctuations as the curved bend (dotted curve). This small offset produces a measured mode conversion using the formulas of Rowe and Waters[25] for backward conversion. We calculate a total mode conversion from the TE^{o}_{01} mode to the TE^{o}_{1n} modes (n = 1, ..., 5) of –45 dB for a 0.4-mm flange offset. While the trapped resonance method cannot yield absolute reflection levels for the various modes of interest, it can give a quick indication of what the total reflection perturbations are relative to free space or to familiar waveguide perturbations such as flange offsets, tilts, and diameter steps. The technique is very sensitive because of the trapping effect of the taper and the component under test. To sweep through all possible resonances within the measurement bandwidth, a length of waveguide can be inserted between the taper and the component under test to increase the number of resonances.

References

1. J. C. Glowienka, J. Vac. Sci. Tech. 18, 1088 (1981).

2. R. S. Symons and H. R. Jory, Advances in Electronic and Electron Physics, Vol. 55, Academic Press (1981).

3. H. R. Jory et al., "Development Program for a 200-kW, cw, 28-GHz Gyroklystron," Quarterly Report Nos. 1-17, July 1976 thru June 1980, prepared by Varian Associates, Inc., under Subcontract Purchase Order No. 53X-01617C for Oak Ridge National Laboratory operated by Union Carbide Corporation for the U. S. Department of Energy Contract W-7405-eng-26.

4. R. A. Dandl et al., Plasma Phys. and Cont. Nucl. Fusion Res., Vol. II, 365 (IAEA, Vienna, 1979).

5. H. O. Eason, Journ. of Microwave Power, Vol. 4, No. 2, 88-99 (1969).

6. R. A. Dandl et al., Plasma Phys. and Cont. Nucl. Fusion Res., Vol. II, 607 (IAEA, Vienna, 1971).

7. S. E. Miller, B.S.T.J., Vol. 33, No. 6, 1209-1265 (1954).

8. J. P. Quine, Microwave Power Engineering, Vol. I, 178-213 (1968), Academic Press, New York (E. C. Okress, ed.).

9. A. P. King and E. A. Marcatili, B.S.T.J., Vol. 35, 899-906 (1956).

10. D. B. Batchelor, Nucl. Fusion 21, 1615-1631 (1981).

11. C. M. Loring, H. O. Eason, H. D. Kimrey, T. L. White (ORNL), H. Jory and S. J. Evans (Varian), IEEE Proc. 9th Symp. on Engr. Prob. of Fusion Res., Vol. 2, 2105-2108 (1981).

12. M. Sucher and J. Fox, Handbook of Microwave Measurements, Polytechnic Press, Vol. I, 179-185 (1963).

13. A. Brown, IEEE Trans. on MTT, Vol. 16, 894 (October 1968).

14. H. R. Jory et al., "Development Program for a 200-kW, cw, 28-GHz Gyroklystron," Quarterly Report No. 17, 21 (June 1980).

15. G. W. Luderer and H. G. Unger, B.S.T.J., Vol. 43, 769 (March 1964).

16. N. Marita and Y. Nakanishi, IEEE Trans. on MTT, Vol. 16, No. 3, 183-189 (1968).

17. C. M. Loring, op. cit., 2107.

18. J. L. Doane, Intl. J. of Electronics, Vol. 53, No. 6, 576-579 (1982).

19. H. R. Jory et al., "Development Program for a 200-kW, cw, 28-GHz Gyroklystron," Quarterly Report No. 17, 17-20 (June 1980).

20. D. A. Everitt, H. O. Eason, R. L. Livesey, and T. L. White, IEEE Proc. 9th Symp. on Eng. Prob. of Fusion Research, Vol. 1, 43-46 (1981).

21. R. A. Lillie, T. L. White, T. A. Gabriel and R. G. Alsmiller, Jr., Nucl. Tech./Fusion 4, 1436-1441 (Sept. 1983).

22. H. Jory et al., "Development Program for a 200-kW, cw, 28-GHz Gyroklystron," Quarterly Report No. 3, 5-7 (Jan. 1977).

23. D. A. Lanciani, IRE Trans., MTT 2, pp. 45-51 (1954).

24. L. Solymar, Proc. IEE (London), Vol. 106, Pt. B, pp. 119-120 (Jan. 1959).

25. H. E. Rowe and W. D. Warters, BSTJ 41, pp. 1151-1153 (1962).

Figure Captions

Fig. 1. The EBT-S 28-GHz, 200-kW, cw, electron cyclotron plasma heating system. (The arrows in the distribution manifold denote net power flow.)

Fig. 2. The ORNL arc detector waveguide section.

Fig. 3. The ORNL high average power waveguide flange.

Fig. 4. A 90°, 40.6-cm radius bend produced by the roll bending technique.

Fig. 5. The EBT-S quasi-optical, mixed-mode, microwave distribution system.

Fig. 6. Correlation of gyrotron output power with power delivered to a dummy load plus intervening waveguide losses.

Fig. 7. A comparison of system performance into a matched load and into the EBT-S ECH plasma.

Fig. 8. The power absorbed by mode absorbers and copper waveguide for (A) a matched load , (B) a window plus matched load, (C) and a window and manifold configuration versus gyrotron output power.

Fig. 9. The power absorbed by the FC-75 and H_2O cooling circuits of the barrier vacuum window for (B) a matched load, and (C) a manifold configuration versus gyrotron output power.

Fig. 10. The cold test setup for the measurement of reflections from oversized waveguide components using the trapped mode resonance technique.

Fig. 11. The TE mode coupler.

Fig. 12. A comparison of trapped mode reflections from a miter bend, a curved bend, and a small flange offset.

ORNL-DWG 83-3130A FED

EBT-S 28 GHz 200 kW CW ECH SYSTEM

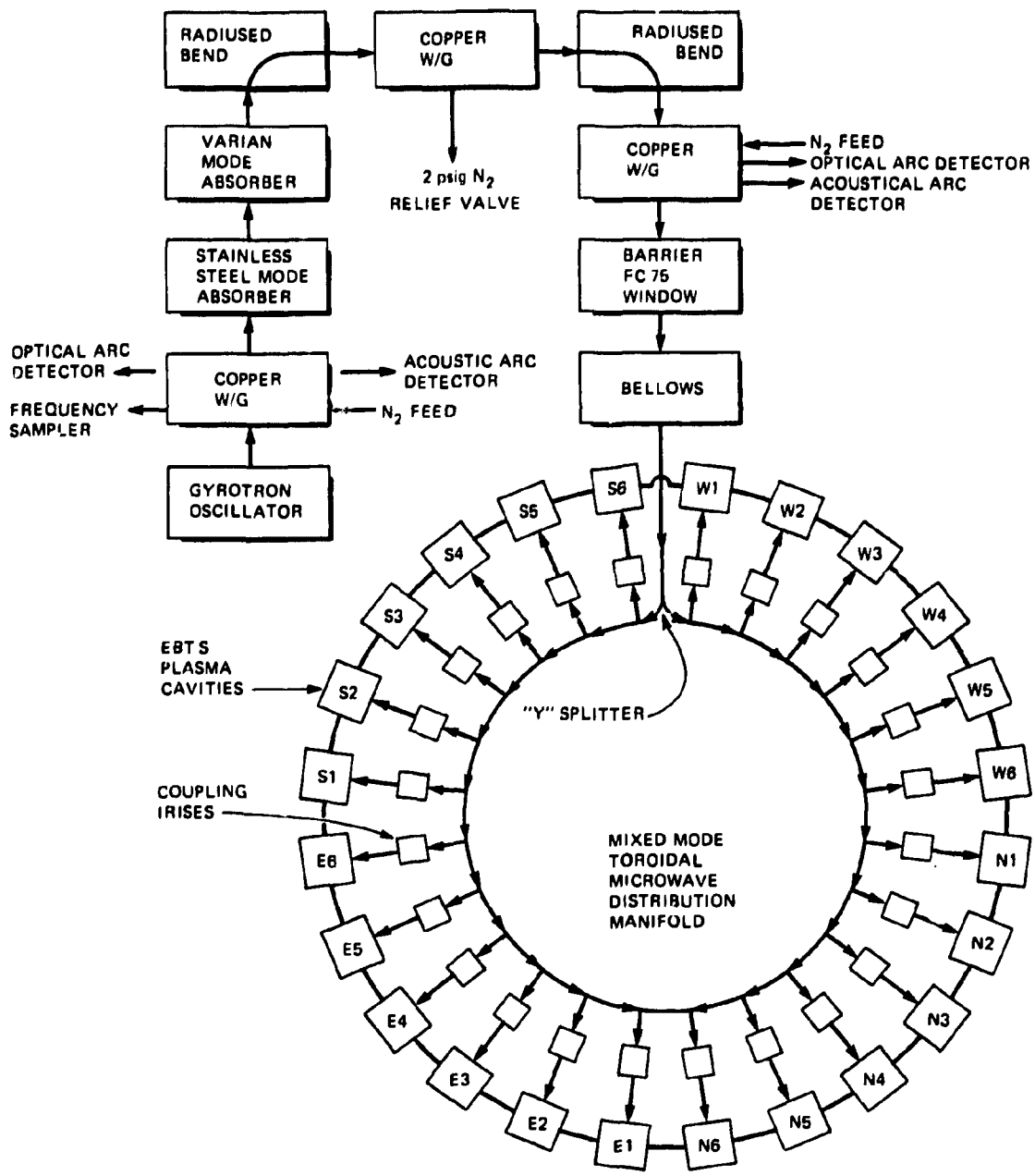

Fig. 1

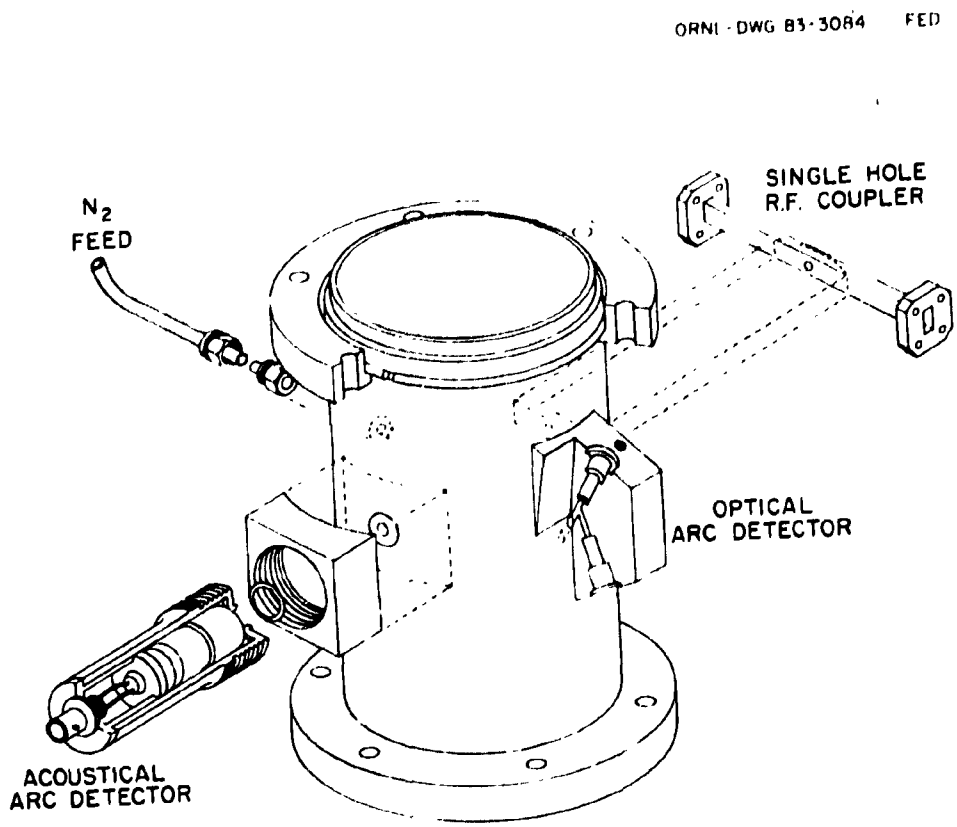
ORNL - DWG 83-3084 FED
N_2
FEED
SINGLE HOLE
R.F. COUPLER
OPTICAL
ARC DETECTOR
ACOUSTICAL
ARC DETECTOR

Fig. 2

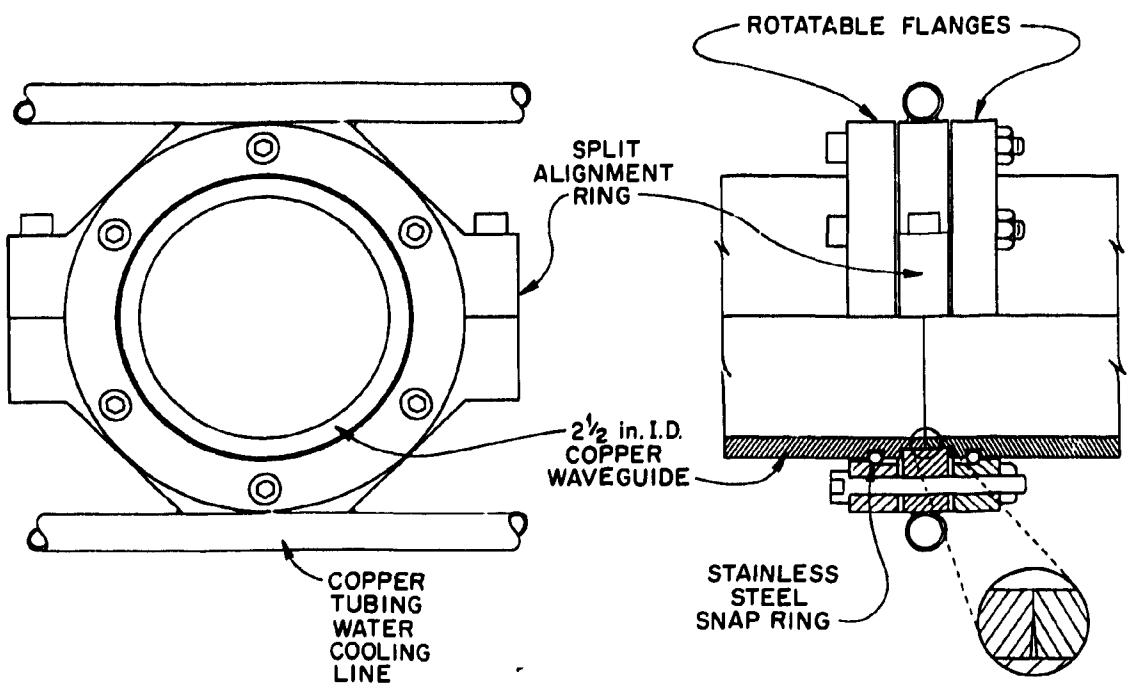
ORNL-DWG 83-3413 FED
ROTATABLE FLANGES
SPLIT ALIGNMENT RING
2½ in. I.D. COPPER WAVEGUIDE
COPPER TUBING WATER COOLING LINE
STAINLESS STEEL SNAP RING

Fig. 3

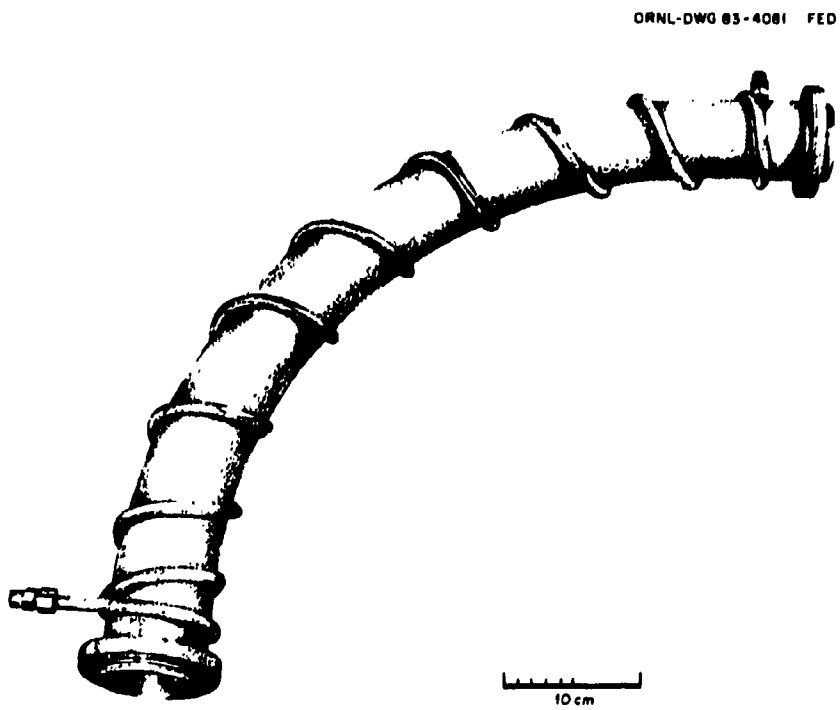

Fig. 4

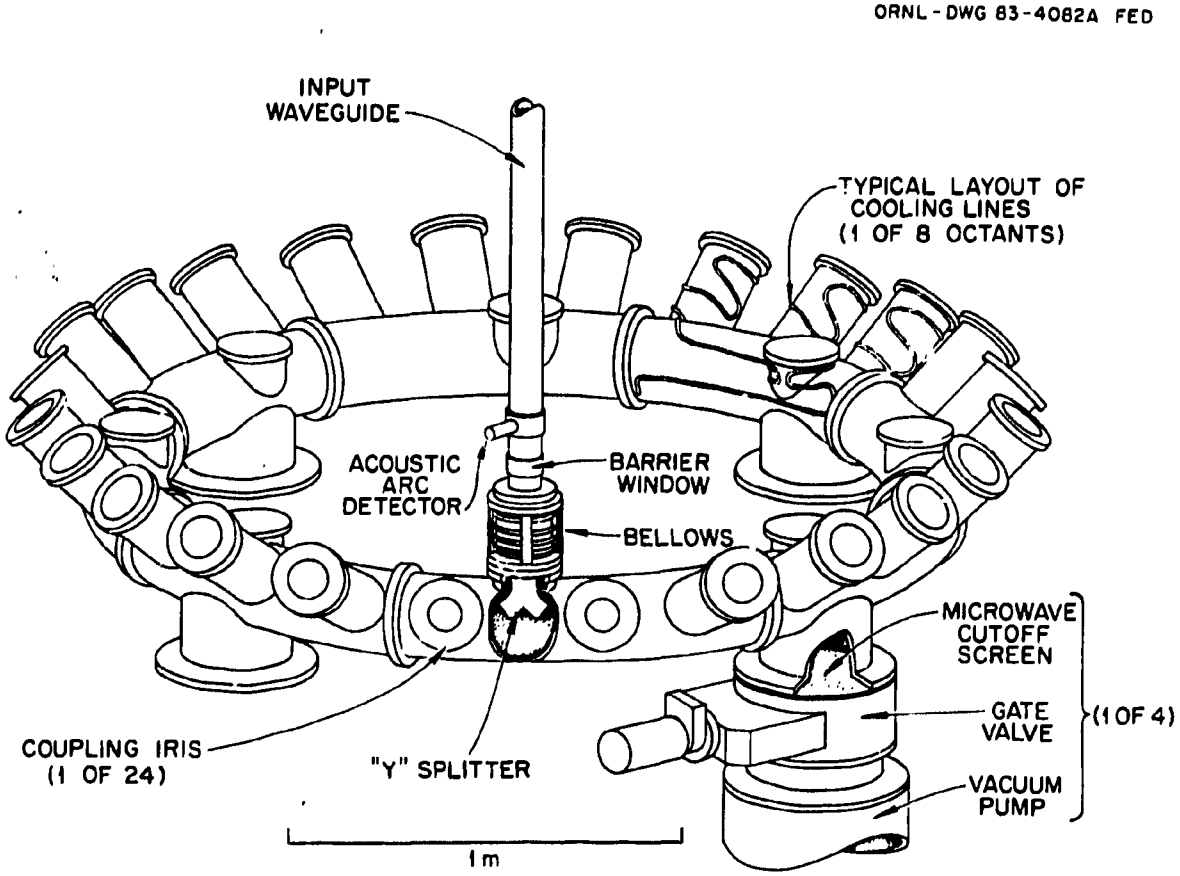
ORNL-DWG 83-4082A FED
INPUT WAVEGUIDE
TYPICAL LAYOUT OF COOLING LINES (1 OF 8 OCTANTS)
ACOUSTIC ARC DETECTOR
BARRIER WINDOW
BELLOWS
MICROWAVE CUTOFF SCREEN
GATE VALVE
(1 OF 4)
VACUUM PUMP
COUPLING IRIS (1 OF 24)
"Y" SPLITTER
1 m

Fig. 5

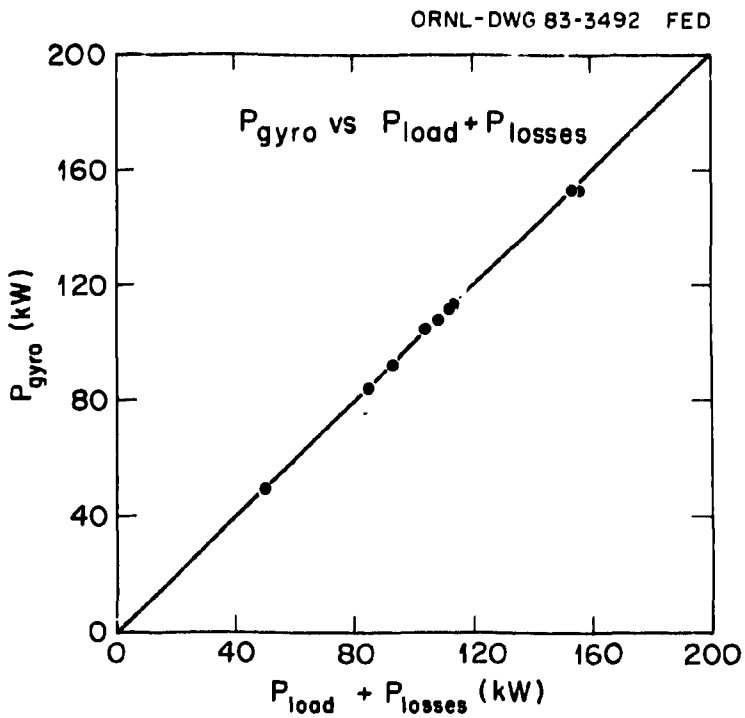
ORNL-DWG 83-3492 FED
P_{gyro} vs $P_{load} + P_{losses}$
200
160
120
80
40
0
0
40
80
120
160
200
P_{gyro} (kW)
$P_{load} + P_{losses}$ (kW)

Fig. 6

EBT-S 28-GHz MICROWAVE SYSTEM PERFORMANCE INTO A MATCHED LOAD AND INTO THE EBT-S PLASMA

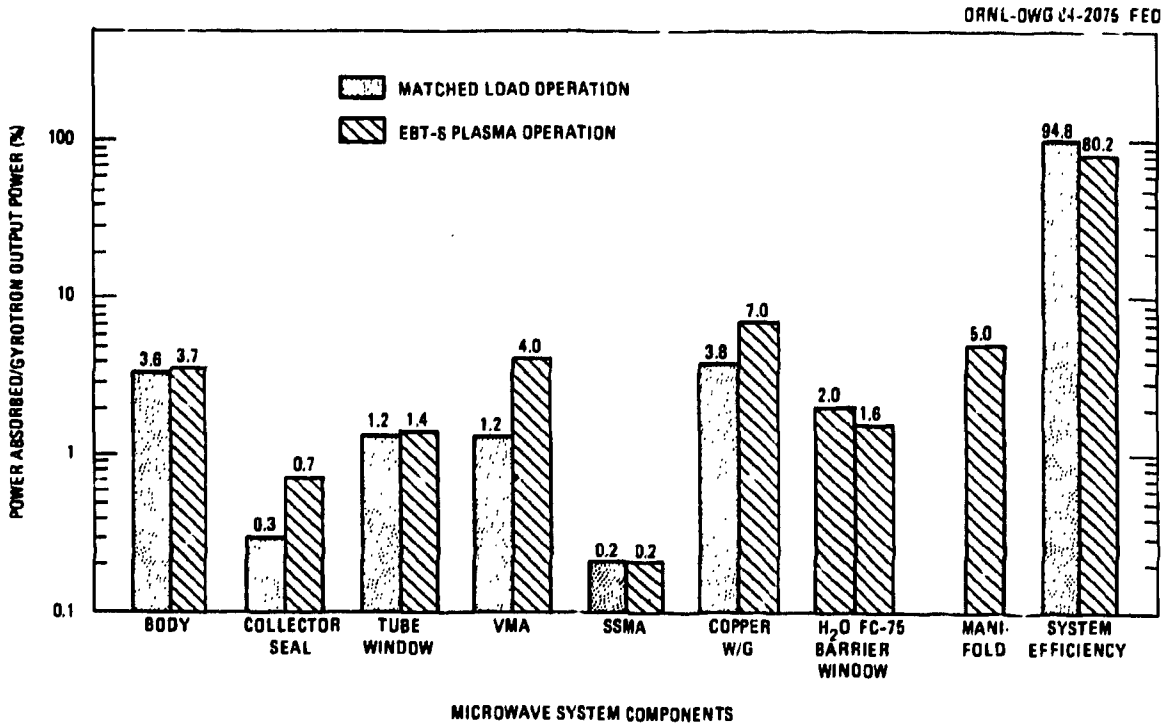

Fig. 7

POWER ABSORBED BY MODE ABSORBERS AND COPPER WAVEGUIDE FOR THREE HOT TEST LOAD CONFIGURATIONS

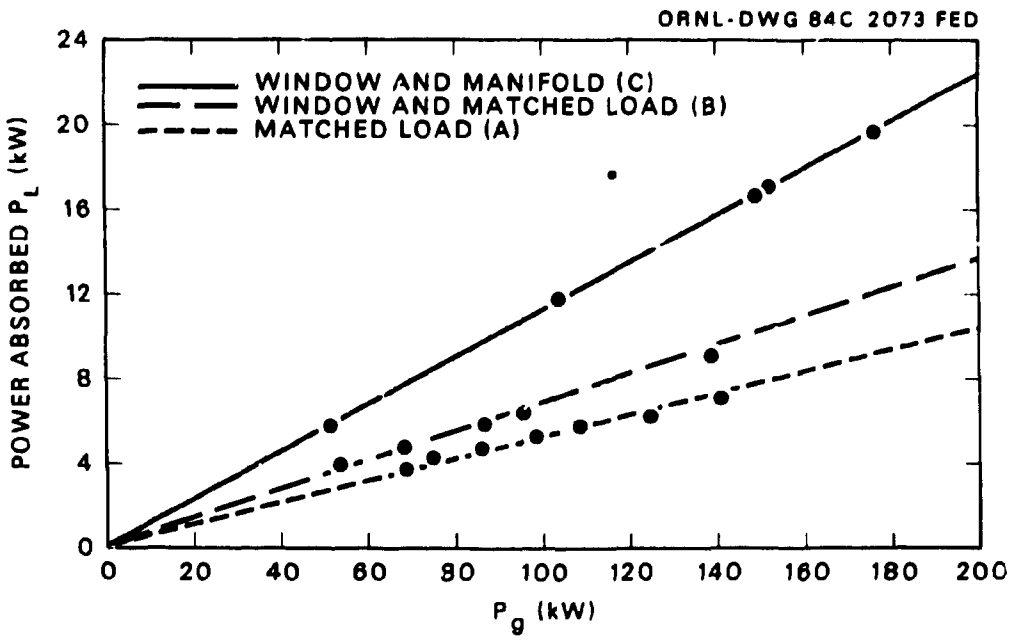

Fig. 8

POWER ABSORBED IN BARRIER WINDOW
FC-75 AND H_2O COOLING CIRCUITS FOR
THREE HOT TEST CONFIGURATIONS

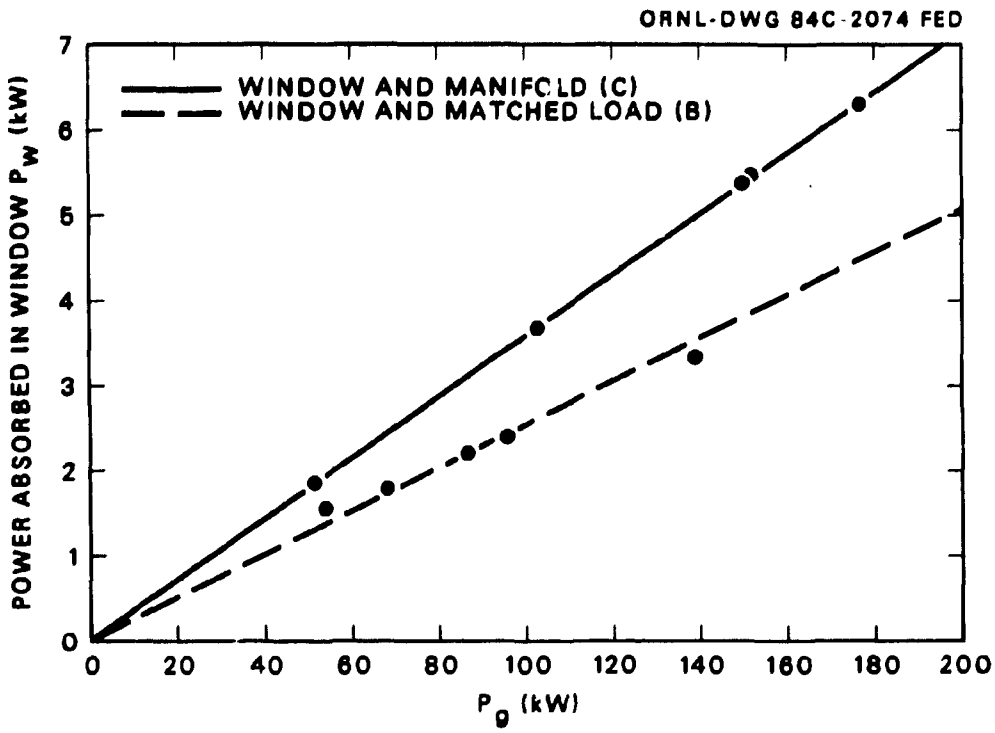

Fig. 9

COLD TEST MEASUREMENT OF RELATIVE REFLECTIONS FROM COMPONENTS

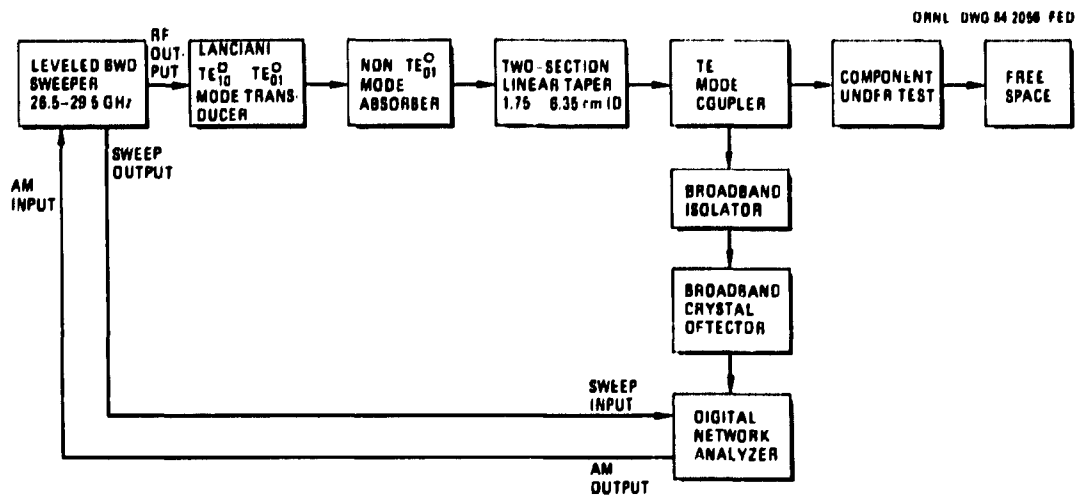

Fig. 10

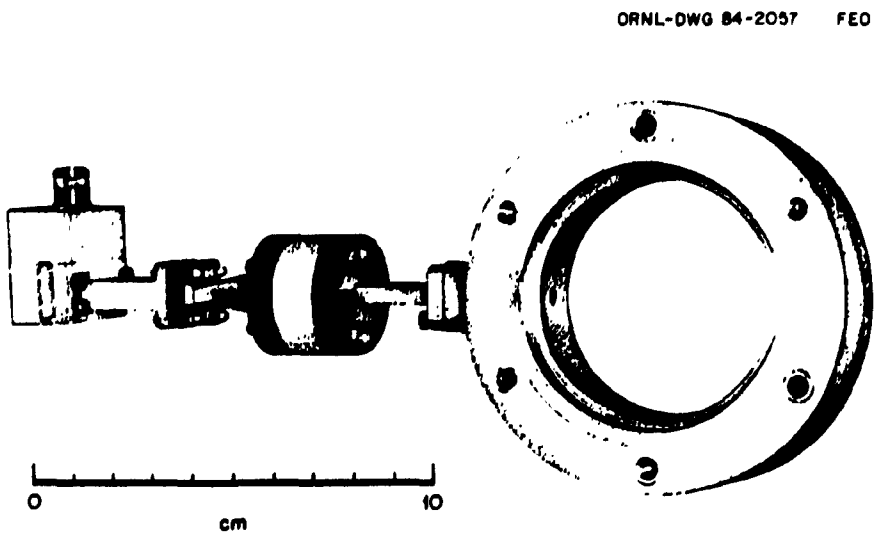

Fig. 11

ORNL/TM-9175
Dist. Category UC-20

INTERNAL DISTRIBUTION

1. F. W. Baity
2. D. B. Batchelor
3-7. D. D. Bates
8. L. A. Berry
9-13. T. S. Bigelow
14. N. B. Bryson
15. J. A. Cobble
16. R. J. Colchin
17. W. A. Davis
18. A. C. England
19. J. C. Glowienka
20. G. R. Haste
21. D. L. Hillis
22. S. Hiroe
23-27. H. D. Kimrey
28. H. C. McCurdy
29. D. H. Metzler
30. D. A. Rasmussen
31. J. Sheffield
32. D. W. Swain
33. T. Uckan
34-38. T. L. White
39-40. Laboratory Records Department
41. Laboratory Records, ORNL-RC
42. Fusion Energy Division Publications Office
43. Central Research Library
44. Fusion Energy Division Library
45. Document Reference Section
46. ORNL Patent Office

EXTERNAL DISTRIBUTION

47. W. B. Ard, McDonnell Douglas Astronautics Company, Bldg. 278, P. O. Box 516, St. Louis, MO 63166
48. H. L. Berk, Institute for Fusion Studies, University of Texas at Austin, RLM 11.218, Austin, TX 78712
49. Bibliothek, Institut fur Plasmaphysik, D-8046 Garching bei Munchen, Federal Republic of Germany
50. Bibliothek, Institut fur Plasmaphysik, KFA, Postfach 1913, D-5170, Federal Republic of Germany
51. Bibliotheque, Service du Confinement des Plasmas, CEA, B.P. No. 6, 92 Fontenay-aux-Roses (Seine), France
52. N. Bowen, Princeton Plasma Physics Laboratory, P. O. Box 451, Princeton, NJ 08540
53. J. D. Callen, Department of Nuclear Engineering, University of Wisconsin, Madison, WI 53706
54. R. W. Conn, School of Engineering and Applied Science, 6291 Boelter Hall, University of California, Los Angeles, CA 90024
55. R. A. Dandl, Applied Microwave Plasma Concepts, 2210 Encinitas Blvd., Suite P, Encinitas, CA 92024.
56. S. O. Dean, Director, Fusion Energy Development, Science Applications, Inc., 2 Professional Drive, Suite 249, Gaithersburg, MD 20760
57. R. J. DeBellis, McDonnell Douglas Astronautics Company, Building 107, P. O. Box 516, St. Louis, MO 63166
58. J. Doane, Princeton Physics Laboratory, P. O. Box 451, Princeton, NJ 08540
59. Documentation S.I.G.N., B.P. 85 Centre de Tri, 38041 Cedex, Grenoble, France
60. A. J. Favale, Grumman Aerospace Corporation, South Oyster Bay Road, P. O. Box 31, Bethpage, NY 11714

61. H. K. Forsen, Bechtel Group, Inc., Research Engineering, P. O. Box 3965, San Francisco, CA 94105
62. M. Fujiwara, Institute of Plasma Physics, Nagoya University, Nagoya 464, Japan
63. T. V. George, Office of Fusion Energy, Office of Energy Research, Mail Station G-256, Department of Energy, Washington, DC 20545
64. G. G. Gibson, Westinghouse Electric Corp., Fusion Power Systems, Dept. C, P. O. Box 10864, Pittsburgh, PA 15236
65. R. W. Gould, Department of Applied Physics, California Institute of Technology, Pasadena, CA 92024
66. H. Hsuan, Princeton Plasma Physics Laboratory, P. O. Box 451, Princeton, NJ 08540
67. H. Ikegami, Institute of Plasma Physics, Nagoya Univ., Nagoya 464, Japan
68. Institute of Physics, Academia Sinica, Peking, Peoples Republic of China
69. H. R. Jory, Varian Associates, 611 Hansen Way, Palo Alto, CA 94303
70. N. A. Krall, Jaycor, 11011 Torreyana Rd., P. O. Box 85154, San Diego, CA 92138
71. K. Krause, Lawrence Livermore National Laboratory, P. O. Box 808, Livermore, CA 94550
72. J. Lassoon, TRW Defense and Space Systems, 1 Space Park, Bldg. R-1, Redondo Beach, CA 92078
73. N. H. Lazar, TRW Defense and Space Systems, 1 Space Park, Bldg. R-1, Redondo Beach, CA 92078
74. Library, Centre de Recherches en Physique des Plasmas, 21 Avenue des Bains, 1007 Lausanne, Switzerland
75. Library, Culham Laboratory, UKAEA, Abingdon, Oxfordshire, OX14-3DB, England
76. Library, FOM Institute voor Plasma-Fysica, Rijnhuizen, Jutphaas, Netherlands
77. Library, Institute for Plasma Physics, Nagoya University, Nagoya 464, Japan
78. Library, International Centre for Theoretical Physics, Trieste, Italy
79. Library, Laboratoria Gas Ionizzati, Frascati, Italy
80. Library, Plasma Physics Laboratory, Kyoto University, Gokasho Uji, Kyoto, Japan
81. D. G. McAlees, Exxon Nuclear Company, Inc., 777 106th Avenue, NE, Bellevue, WA 98009
82. J. B. McBride, Science Applications, Inc., 1200 Prospect Street, P. O. Box 2351, La Jolla, CA 92037
83. C. Moeller, General Atomic Company, 10955 John Jay Hopkins Drive, San Diego, CA 92121
84. Plasma Research Laboratory, Australian National University, P. O. Box 4, Canberra ACT, 2000, Australia
85. P. J. Reardon, Princeton Plasma Physics Laboratory, P. O. Box 451, Princeton, NJ 08544
86. F. L. Ribe, College of Engineering, AERL Building, FL-10, University of Washington, Seattle, WA 98195
87. T. E. Romesser, TRW Defense and Space Systems, 1 Space Park, Bldg. R-1, Rm 2020, Redondo Beach, CA 92078
88. W. M. Stacey, School of Nuclear Engineering, Georgia Institute of Technology, Atlanta, GA 30332
89. B. W. Stallard, Lawrence Livermore National Laboratory, P. O. Box 808, Livermore, CA 94550
90. Thermonuclear Library, Japan Atomic Energy Research Institute, Naka, Ibaraki, Japan
91. J. M. Turner, Office of Fusion Energy, Office of Energy Research, Mail Station G-256, Department of Energy, Washington, DC 20545
92. R. Varma, Physical Research Laboratory, Navrangpura, Ahmedabad, India

93. H. Weitzner, New York University, Courant Institute of Mathematical Sciences, 251 Mercer Street, New York, NY 10012.
94. Office of the Assistant Manager for Energy Research and Development, Oak Ridge Operations Office, Department of Energy, P. O. Box E, Oak Ridge, TN 37830
95-200. Given distribution as shown in TID-4500, Magnetic Fusion Energy (Distribution Category UC-20)

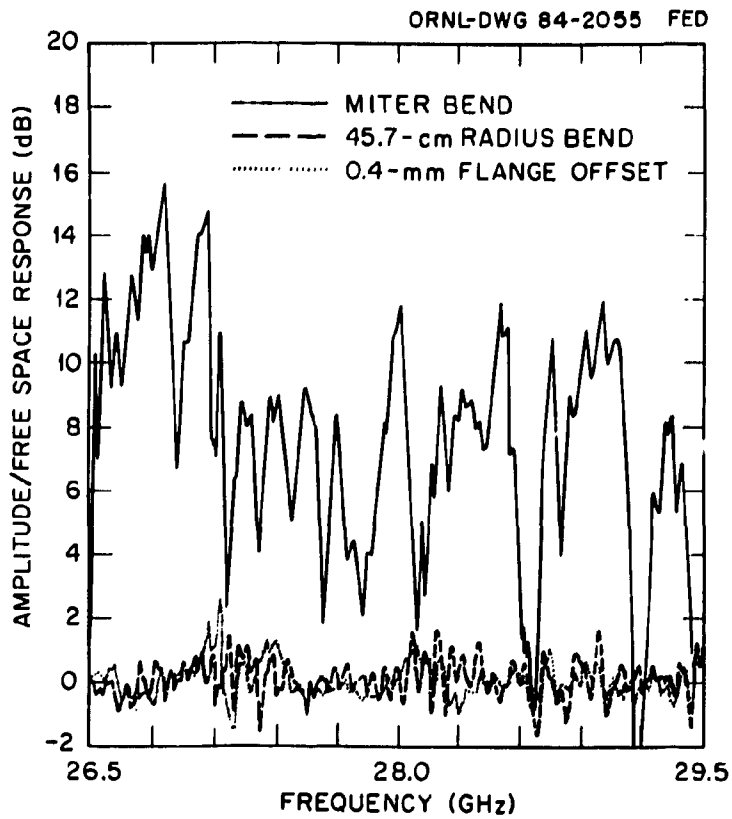
ORNL-DWG 84-2055 FED
MITER BEND
45.7-cm RADIUS BEND
0.4-mm FLANGE OFFSET
AMPLITUDE/FREE SPACE RESPONSE (dB)
20
18
16
14
12
10
8
6
4
2
0
-2
26.5
28.0
29.5
FREQUENCY (GHz)

Fig. 12